AIAA 2001-0648
Performance Modeling Of Experimental Laser Lightcrafts

Ten-See Wang
NASA Marshall Space Flight Center
Huntsville, AL

Yen-Sen Chen and Jiwen Liu
Engineering Sciences, Inc.
Huntsville, AL

Leik N. Myrabo
Rensselaer Polytechnic Institute
Troy, NY

Franklin B. Mead, Jr.
Air Force Research Laboratory
Edwards AFB, CA

39th AIAA Aerospace Sciences Meeting & Exhibit
8-11 January 2001 / Reno, NV

Performance Modeling of Experimental Laser Lightcrafts

Ten-See Wang*
NASA Marshall Space Flight Center, Huntsville, AL 35812
Yen-Sen Chen† and Jiwen Liu‡
Engineering Sciences, Inc., Huntsville, AL 35802
Leik N. Myrabo§
Rensselaer Polytechnic Institute, Troy, NY 12180
and
Franklin B. Mead, Jr.**
Air Force Research laboratory, Edwards AFB, CA 93524

Abstract

A computational plasma aerodynamics model is developed to study the performance of a laser propelled Lightcraft. The computational methodology is based on a time-accurate, three-dimensional, finite-difference, chemically reacting, unstructured grid, pressure-based formulation. The underlying physics are added and tested systematically using a building-block approach. The physics modeled include non-equilibrium thermodynamics, non-equilibrium air-plasma finite-rate kinetics, specular ray tracing, laser beam energy absorption and refraction by plasma, non-equilibrium plasma radiation, and plasma resonance. A series of transient computations are performed at several laser pulse energy levels and the simulated physics are discussed and compared with those of tests and literatures. The predicted coupling coefficients for the Lightcraft compared reasonably well with those of tests conducted on a pendulum apparatus.

Nomenclature

A_j	reaction rate constant of the j-th reaction
A_p, A_m	matrix coefficients of transport equations
c	speed of light in a vacuum.
D	species diffusivity
e_v	vibrational energy
e_v^{eq}	equilibrium vibrational energy
$\vec{F}$	flux vector
g_i	Gibbs' free energy of species i
H	total enthalpy
I	intensity or number of quantum levels
j	emission coefficient
K	transfer constant between quantum levels
k_b	Boltzmann's constant
k_c	Coulomb constant
k_v	thermal conductivity
M_w	molecular weight
m_e	electron mass
N	total quantum level population
N_i	quantum level
n	refraction index
$\vec{n}$	unit normal vector
n_e	electron number density
P_r	Prantdl number
p	gas static pressure
p_e	partial electron temperature
Q_c	collision energy transfer
Q_r	net radiative heat flux
q_e	electron charge
R	gas constant

* Staff, Senior Member AIAA
† President, Member AIAA
‡ Senior Research Engineer, Member AIAA
§ Associate Professor, member AIAA
** Senior Scientist, Member AIAA

$\vec{r}$	position vector
S	source terms
T	gas temperature, K
T_e	electron temperature, K
T_t	translational temperature, K
T_v	vibrational temperature, K
t	time, s
u_i	velocity components
V	velocity magnitude
x_i	Cartesian coordinates
Y_i	chemical species mass fraction

Greek Symbols

ε_0	permittivity
ϕ	dependent variable
Γ	control surface
κ_l	laser absorption coefficient.
λ_e	electron species thermal conductivity
λ_l	laser wavelength
μ	viscosity
ν_{ij}	stoichiometric coefficient
θ	refractive angle
ρ	density
τ_{LT}	vibrational-translational relaxation time scale
τ_{ij}	shear stress tensor
Ω	control volume domain
$\dot{\omega}_i$	chemical reaction source term
ω_p	plasma frequency

Introduction

Beamed energy propulsion was first promoted by Kantrowitz[1]. Since then, a propulsion system supported by a laser-sustained plasma has been the subject of many studies.[2-6] The main advantage gained by laser propulsion is the low-weight system derived from decoupling the energy source from the vehicle, and high specific impulse resulting in low fuel consumption. The first ground and flight tests of a ground-based laser propelled vehicle were reported in 1998,[7] in which active tracking and beam control were demonstrated to 122 m on a horizontal wire and spin-stabilized free flights in the laboratory were accomplished to altitude of 4 m. Six months later, the spin-stabilized vertical free flights outdoors reached 30 m.[8] These results were accomplished with axisymmetric vehicles which are of a special design in which a nosecone shaped forebody, an annular shroud, and a parabolic afterbody are the only major components. A vehicle of such design is hereby named as the "Laser Lightcraft" in this study. The layout of a computational grid for a Laser Lightcraft is shown in Fig. 1. The parabolic afterbody surface serves both as an aerospike nozzle and also the main receiving optic, whereas the annular shroud surrounds the ring focus of the parabolic optic. The Laser Lightcraft uses a Rocket-Based Combined Cycle (RBCC) to operate in both the rocket and air-breathing modes. When operating in an air-breathing mode, the specific impulse is infinity since no fuel is consumed. These successful tests[7,8] demonstrated the concept and the potential feasibility of launching small payload with a Laser Lightcraft.

When the focused beam energy strikes the shroud of a Laser Lightcraft, free electrons form to invoke Inverse Bremsstrahlung (IB) and the optical breakdown ensues. In order to achieve maximum intensity and to avoid plasma resonance, repetitive short pulses are used. As such, repetitive Pulsed Detonation Waves (PDW) are generated to propel the vehicle, hence the Laser Lightcraft engine is also known as a PDW engine. It can be seen that the underlying physics involved such as IB and PDW are so complicated that a simple system model is not capable of describing the phenomena, let alone predicts the thrust performance and the associated flow and thermal environments necessary for designing for the structure integrity. A detailed computational plasma aerodynamics model is therefore needed for the design and scaling of future Laser Lightcrafts.

From May to July, 1999, performance data in the form of coupling coefficients were taken in a series of indoor tests for the Model #200 series vehicles. These test were performed under a cooperative effort between Rensselaer Polytechnic Institute, the Air Force Research Laboratory's Propulsion Directorate and NASA's Marshall Space Flight Center (MSFC), to enhance Laser Lightcraft propulsion research. These data are the first of a kind benchmark quality data for computational model development. Armed with these data for comparison purposes, a computational plasma aerodynamics methodology is developed as a first attempt to predicting the thrust performance of a PDW engine propelled Laser Lightcraft.

Computational Plasma Aerodynamics Development

Several attempts have been made to analytically or computationally model the physics inside continuous wave (CW) devices. For example, an early effort by Raizer[9] assumed constant-pressure one-dimensional (1D) flow in air with heat addition by a laser. Thermal conduction was considered dominant and the radiation loss from the plasma was ignored. Kemp and Root[10] later extended this 1D analysis to hydrogen and to include thermal radiation. Molvik, Choi, and Merkle[5] extended this problem to a two-dimensional (2D) structured-grid hydrogen flow and implemented real ray tracing, but ignored thermal radiation. Jeng and Keefer[4] did similar analysis and added thermal radiation. Myrabo, Raizer, and Surzhikov[6] later simulated the radiative-gasdynamics processes in optical discharges

maintained in a subsonic De Laval nozzle. In the work described in this paper, a multidimensional unstructured-grid computational plasma aerodynamics methodology is developed for both CW and repetitively pulsed wave devices, with emphases on nonequilibrium effects and laser-induced physics such as laser–plasma interactions. Realistic laser absorption coefficients are used. The governing equations will be described first, with the auxiliary equations that compute the nonequilibrium and laser induced physics to follow.

The Governing Equations

To properly describe the plasma aerodynamics involved in laser propelled propulsion, the time-varying transport equations of continuity, species continuity, momentum, global energy (total enthalpy) and electron energy are formulated and written in a Cartesian tensor form:

$$\frac{\partial \rho}{\partial t}+\frac{\partial}{\partial x_j}\left(\rho u_j\right)=0$$

$$\frac{\partial \rho Y_i}{\partial t}+\frac{\partial}{\partial x_j}\left(\rho u_j Y_i\right)=\frac{\partial}{\partial x_j}\left[\left(\rho D\right)\frac{\partial Y_i}{\partial x_j}\right]+\dot{\omega}_i$$

$$\frac{\partial \rho u_i}{\partial t}+\frac{\partial}{\partial x_j}\left(\rho u_j u_i\right)=-\frac{\partial p}{\partial x_i}+\frac{\partial \tau_{ij}}{\partial x_j}$$

$$\frac{\partial \rho H}{\partial t}+\frac{\partial}{\partial x_j}\left(\rho u_j H\right)=\frac{\partial p}{\partial t}+Q_c+\frac{\partial}{\partial x_j}\left(\frac{\mu}{P_r}\nabla H\right)+\frac{\partial}{\partial x_j}\left[\left(1-\frac{\mu}{P_r}\right)\nabla\left(V^2/2\right)\right]$$

$$\frac{\partial}{\partial t}\left(\frac{2}{3}k_h n_e T_e\right)+\frac{\partial}{\partial x_j}\left(\frac{2}{3}k_h n_e T_e u_j\right)=\frac{\partial}{\partial x_j}\left(\lambda_e\frac{\partial T_e}{\partial x_j}\right)+Q_r-Q_c$$

where the shear stress τ_{ij} can be expressed as:

$$\tau_{ij}=\mu\left(\frac{\partial u_i}{\partial x_j}+\frac{\partial u_j}{\partial x_i}-\frac{2}{3}\frac{\partial u_k}{\partial x_k}\delta_{ij}\right)$$

The beam energy absorption, beam energy transfer, and plasma radiation are invoked through the source terms of the global energy and the electron energy equations, whereas the plasma species are generated through the source terms of the species continuity equations.

Numerical Scheme

The cell-centered scheme is employed to allow the volume surfaces to be represented by the grid cell surfaces. The transport equations can be written in integral form as:

$$\frac{\partial}{\partial t}\int_\Omega \rho\phi\, d\Omega+\oint_\Gamma \vec{F}\cdot\vec{n}\, d\Gamma=\oint_\Omega S_\phi\, d\Omega$$

where Ω is the domain of interest and Γ denotes the surrounding surfaces; $\vec{n}$ is a unit normal vector of Γ in the outward direction. The flux function $\vec{F}$ contains the inviscid and the viscous flux vectors.

$$\vec{F}=\rho\vec{V}\phi-\mu_\phi\nabla\phi$$

Let's consider a control volume interface, e, between control volumes E and P, with a normal vector n. And, $\phi_E-\phi_P=\overline{\nabla\phi}_e\bullet\left(\vec{r}_E-\vec{r}_P\right)$, where $\overline{\nabla\phi}_e$ is interpolated from the neighbor cells E and P. For the face e between control volumes P and E, the diffusive flux can be approximated as:

$$\left(\nabla\phi\bullet\vec{n}\right)_e\approx\frac{\phi_E-\phi_P}{\left|\vec{r}_E-\vec{r}_P\right|}+\overline{\nabla\phi}_e\bullet\left(\vec{n}-\frac{\vec{r}_E-\vec{r}_P}{\left|\vec{r}_E-\vec{r}_P\right|}\right)$$

The finite volume formulation of flux integral can be evaluated by the summation of the flux vectors over each face,

$$\oint_\Gamma \vec{F}\cdot\vec{n}\, d\Gamma=\sum_{j=k(i)}F_{i,j}\,\Delta\Gamma_j$$

where k(i) is a list of faces of cell i, $F_{i,j}$ represents convection and diffusion fluxes through the interface between cell i and j, and $\Delta\Gamma_j$ is the cell-face area.

The convective flux is evaluated through the upwind-cell quantity by a linear reconstruction procedure to achieve second order accuracy: $\phi_e=\phi_u+\phi_e\nabla\phi_u\bullet\left(\vec{r}_e-\vec{r}_u\right)$ where the subscript u represents the upwind cell and ψ_e is a limiter used to ensure that the reconstruction does not introduce local extrema. The limiter proposed by Barth[11] is used here. Defining $\phi_{max}=max(\phi_u,\phi_j)$, $\phi_{min}=min(\phi_u,\phi_j)$ (and assuming ϕ_e^0 is computed with $\psi_e=1$) the scalar ψ_e associated with the gradient at cell u due to edge e is:

$$\psi_e=\begin{cases}min\left(1,\dfrac{\phi_{max}-\phi_u}{\phi_e^0-\phi_u}\right) & if\ \phi_e^0-\phi>0\\ min\left(1,\dfrac{\phi_{min}-\phi_u}{\phi_e^0-\phi_u}\right) & if\ \phi_e^0-\phi<0\\ 1 & if\ \phi_e^0-\phi=0\end{cases}$$

Solution Procedures

A general implicit discretized time-marching scheme for the transport equations can be written as below,

$$\left(\frac{\rho^n}{\Delta t}+A_p\right)\phi_p^{n+1}=\sum_{m=1}^{NB}A_m\phi_m^{n+1}+\frac{(\rho\phi_p)^n}{\Delta t}+S_\phi$$

where *NB* means the neighbor cells of cell P. The high order differencing term and cross diffusion term are treated using known quantities and retained in the source term and updated explicitly. The second term of the right-hand side (RHS) is a perturbation that comes from the RHS. A predictor and corrector solution algorithm is employed to provide coupling of the governing equations. The discretized finite-volume equations form a set of linear algebraic equations, which are non-symmetric matrix system with arbitrary sparsity patterns. The preconditioned Bi-CGSTAB[12] and GMRES(m)[13] matrix solvers are used to efficiently solve the linear algebraic equations.

Auxiliary Equations

Thermal Non-Equilibrium Energy Equations

For high temperature flows, thermal non-equilibrium state may be important. In Landau and Teller's derivation,[14] a master equation is employed to describe the evolution of the population of quantum level N_i. This master equation is written as:

$$\frac{dN_i}{dt}=N\sum_{j=0}^{I_{\max}}K_{j\Rightarrow i}N_j-N\sum_{j=0}^{I_{\max}}K_{i\Rightarrow j}N_i;i=0,1,2,\ldots,I_{\max}$$

Results from the quantum mechanical solution of the harmonic oscillator are used to relate the various quantum transition rates to one another, and then the master equation may be summed over all quantum states to obtain the Landau-Teller equation:

$$\frac{D\rho e_v}{Dt}=\frac{\partial}{\partial x_i}\left(k_v\frac{\partial T_v}{\partial x_i}\right)+\rho\frac{e_v^{eq}(T_t)-e_v}{\tau_{LT}}$$

An empirical expression (given below) is used to model the Landau-Teller relaxation time scale. The Landau-Teller expression for the vibrational relaxation time is calculated using the 6-coefficient specified.

$$\tau_{LT}=\frac{b_1T^{b_2}\exp\left[(b_3/T)^{b_4}\right]}{p(1-b_5\exp(-b_6/T))}$$

where b_1=7.1E-4, b_2=0, b_3=1.91E6, b_4=0.3333, b_5=0, b_6=0 are used here. To solve this vibrational energy equation, the source term is linearized to result in an explicit term and an implicit term. This treatment is important for an unconditionally stable solution of the equation. That is,

$$\text{Explicit source term} = \rho\frac{e_v^{eq}(T_t)}{\tau_{LT}}$$

$$\text{Implicit source term} = -\frac{\rho}{\tau_{LT}}e_v$$

The vibrational temperature is used to influence the reaction rates of chemical reactions by assuming that the rate coefficients for dissociation are functions of the geometrical mean temperature between T and T_v.[15]

Non-Equilibrium Air Chemistry

A general system of chemical reactions can be written in terms of its stoichiometric coefficients (v_{ij} and v_{ij}') and the i^{th} chemical species name (M_i) of the j^{th} reaction as

$$\sum_i \upsilon_{ij}'M_i=\sum_i \upsilon_{ij}M_i$$

The net rate of change in the molar concentration of species i due to reactions j, X_{ij}, and the species production rate can be written as:

$$X_{ij}=\left(\upsilon_{ij}-\upsilon_{ij}'\right)\left[K_{fj}\prod_i\left(\frac{\rho Y_i}{M_{wi}}\right)^{\upsilon_{ij}'}-K_{bj}\prod_i\left(\frac{\rho Y_i}{M_{wi}}\right)^{\upsilon_{ij}}\right]$$

$$\dot{\omega}_i=M_{w_i}\sum_j X_{ij}$$

The forward (Arrhenius law) and backward reaction rates for each reaction is given by:

$$Kf_j=A_jT^{B_j}Exp\left(-\frac{E_j}{RT}\right)$$

$$Kb_j=\frac{Kf_j}{Ke_j}$$

where Ke_j is the equilibrium coefficient

$$Ke_j=(RT)^{-\sum_{i=1}^{n}(v_{ij}''-v_{ij}')}Exp\left[-\frac{\sum_{i=1}^{n}(v_{ij}''-v_{ij}')g_i}{RT}\right]$$

A point-implicit (operator splitting) method is employed to solve the chemistry system. For the breakdown of air, Park's multitemperature air chemistry[15] is baselined in this study. This mechanism composes of

the dissociation, NO exchange, associative ionization, charge exchange, electron-impact ionization, and radiative recombination reactions. With this mechanism, electrons are produced first by the associative ionization process and more electrons are produced by the electron-impact reactions. Since the number of electrons doubles in each such event, electron density increases exponentially, in the form of an avalanche.[15] This mechanism thus provides the initial electron density for ignition and produces the avalanche of electrons necessary for the subsequent optical breakdown. It can be seen that the IB process is embedded in the dissociation, associative ionization, and electron-impact ionization reactions. The reaction rates were validated[15] with experiments of postshock temperatures ranging from 20,000 – 60,000 K which are inline with the maximum computed breakdown temperatures.

Plasma Initiation

Understanding the mechanisms responsible for plasma initiation (ignition) has been the subject of ongoing research. A spark gap, an extremely intense pulse of laser energy striking the focal point, seeded molecules or particles, or a retractable tungsten target placed at the focal point[16] have been used as sources of free electrons for initiation.[2] It has also been shown that plasma can be ignited quite easily off metal surfaces.[2] Likewise in numerical modeling, initial free electrons are required for plasma ignition. This means determining an initial electron density or a threshold breakdown intensity. For example, Ergun[16] described an initial electron density that is necessary for modeling the ignition of a hydrogen plasma initiated with a retractable tungsten wire. In this study, a threshold breakdown intensity approach is devised in anticipation that a different threshold breakdown intensity may be encountered for differing surface material, target approach, and laser power. The advantage of this approach is that the threshold breakdown intensity can either be calibrated or measured. For example, the effect of seeds on laser breakdown intensity has been reported.[2] In this study, this approach is accomplished by performing parametric studies on plasma initiation with spark time, spark region, and spark power. A "spark" provides a fixed amount of energy (spark energy) in a region (spark region) centered around the focal point for a fixed amount of time (spark time). When the strength of a spark reaches a threshold, or the threshold breakdown intensity is satisfied, a laser supported combustion (LSC) or detonation (LSD) is initiated.

That means enough seed electrons are produced through the likes of associative ionization reactions such that the subsequent optical breakdown (ignition) is possible. It is found that an ignition is sustainable when the energy absorbed by the plasma reaches 15% of that delivered. Spark times computed based on that criterion range from 0.4 μs to 1.2 μs. As expected, lower laser pulse energies require longer spark times for ignition. It is also reasonable to assume that the plasma initiates in a (spark) region enclosed by the two outer laser rays and an arc with an origin at the focal point (in a 2D sense), and the (spark) radius of that region is determined empirically as 1 mm. In actuality, the spark region is a torus generated by a pie-shaped cross-section rotated about the vehicle axis. Finally, the spark power is also empirically determined as 15% of that of the incident laser – its theoretical maximum.

Laser Radiation

Geometric optics is used to simulate the local intensity of the laser beam, which is split into a number of individual rays. In the presence of absorption, the local intensity of each ray follows the Beer's law:

$$\frac{dI_i}{ds_i} = -\kappa_l I_i$$

The electron is the only plasma species that absorbs the laser energy. The absorption coefficient of the CO_2 laser radiation, corrected for stimulated emission in the single ionization range, is approximated by the formula:[17]

$$\kappa_{lCO_2} = \frac{5.72 p_e^{\,2} \ln[27(T/10^4)^{4/3} p_e^{\,-1/3}]}{(T/10^4)^{7/2}}$$

A ray may change its propagating direction due to the inhomogeneous refractive index within the hot plasma. The index of refraction is taken from Edwards and Pleck:[18]

$$n = \left[1 - \left(\frac{n_e \lambda_l q_e k_c}{m_e c^2 \pi}\right)\right]^{1/2}$$

The refracted angle is associated with the refractive index through the Snell's law:[19]

$$n_1 \sin\theta_1 = n_2 \sin\theta_2$$

where n_1 and n_2 represent the refractive indexes for two different control volumes, and θ_1 and θ_2 are the incident and refracted directions with respect to the normal direction of the interface between two volumes.

experiments. The CO_2 laser delivered up to 400 J single-pulses at a pulse width of 18 μs. The laser pulse energy was measured with a calorimeter and the uncertainty of the delivered energy was estimated to be ± 10 J. Several variations of the basic Laser Lightcraft design (Model 200 series) similar to those described in Ref. 8 were examined and the test results of the 6061-T6 all aluminum Model #200-3/4 vehicle and Model A vehicle are chosen for this study. The vehicle shape of Model A can be found in Ref. 7. The impulse measurements were conducted with a pendulum apparatus. This technique employed a velocimeter coil, which was used in previous work to determine the impulse imparted to a flat plate using the PHAROS III laser at Naval Research Laboratory.[30] The Laser Lightcraft was suspended and suitably weighed before being subjected to a single pulse of energy from the PLVTS laser. The uncertainty in the impulse measurement is estimated to be 1% or better. Details of the laser, measurement technique, and pendulum apparatus can be found in Refs. 7 and 8.

Computational Grid Generation

Figure 1 shows the layout of a computational grid (for Model #200-3/4). As described in Refs. 7 and 8, the Laser Lightcraft vehicle consists of a forebody (nose), an annular shroud, and a PDW engine (parabolic optic). Only half of the grid shown in Fig. 1 is actually solved due to the axisymmetric formulation. An eight-zone structured grid was generated first using a grid generation code called UMESH.[31] The grid is then fed to an auxiliary program such that an one-zone unstructured-grid is constructed for the actual computation. Quadrilateral elements are used such that the wall boundary layer can be computed if needed. High grid density is used in the inner shroud region for capturing the optical breakdown and pulsed detonation wave processes.

Results and Discussion

A series of computations have been performed for average laser pulse energies of 75, 100, 150, 200, 300 and 400 J for Model #200-3/4, and 400, 600, and 800 J for Model A. Maximum computed temperatures ranging from 51,000 to 60,000 K fall within the computed post-shock temperatures of 20,000 to 60,000 K using Park's multi-temperature air chemistry.[15] LSD occurs in all cases with maximum Mach number reaching 2.5. LSC then ensues as the plasma front expands, and the Mach number decreases to subsonic value. Figure 2 shows the computed temperature contours and laser beam traces at an elapsed time of 10 μs and an average laser pulse energy of 400 J. It can be seen that the laser beam reflects specularly on the optical surface and focuses onto a focal "point" on the shroud where the breakdown of air starts. Ten laser rays are plotted for clarity, whereas two hundred rays are actually used in the computation.

It is probably best to recount the phenomenon of an optical detonation wave, which is a detonation wave generated by the optical breakdown of a medium with an incident laser beam, at this moment. This was put forward by Raizer[17] in detail in his book. Essentially, a strong shock wave is generated in the region where the laser radiation that produces the plasma is absorbed and heat is deposited very rapidly. This shock wave travels through the medium, heating and ionizing it such that the medium becomes capable of absorbing more laser radiation. The laser energy is deposited in successive layers of a medium adjoining the front of the shock wave subjected to the laser radiation. These layers themselves thus become energy sources that maintain the shock wave. Hence, the shock wave moves along the optical channel in the opposite direction to the laser beam. Thus, during the initial stages the shock wave is maintained by the laser beam and does not decay.

In Fig. 2 the optical breakdown is being fed by the laser energy and the plasma front grows. Notice the rays are allowed to bend as the index of refraction varies with the expanding plasma. As the local electron density of a plasma front reaches the critical value such that plasma resonance occurs, the local plasma becomes opaque and the regular laser energy absorption is greater on other points of the surface of the plasma front. This process is nonlinear and may explain the irregular shape of the plasma front. It is anticipated that eventually the laser beam is totally reflected as the plasma resonance phenomenon spreads over the entire plasma front. The phenomenon of plasma resonance disappears as the plasma front expands and the electron density decreases. The computed optical breakdown phenomenon appears to agree with the description given by Raizer.[17] Notice that the spreading of the shock wave outside the optical channel results in gradual attenuation because there is no energy to maintain it. Thus, as the shock wave expands in the direction opposite to the laser beam, it is weakly maintained by laser radiation when it is not in a state of plasma resonance.

Figure 3 shows the temperature contours at an elapsed time of 20 μs. At this time, the laser beam is turned off since the pulse width is fixed at 18 μs, thus the shock wave is not being maintained by the laser radiation. The computational results show that a pulsed detonation wave usually takes place at approximately 10 to 20 μs after the start command. The higher the pulse energy, the earlier the generation of a pulsed detonation wave. Part of this propagating detonation wave will hit the parabolic optic and reflect off the surface. The reflected and non-reflected portions would combine to make a propagating Mach stem. It should be noted that the phenomenon of a

propagating Mach stem on the optical surface is very similar to that of a propagating Mach disc inside a bell nozzle during the start-up transient.[32,33] This is because the aerospike optic geometry is an "inside-out" version to that of a contoured bell nozzle.

As the Mach stem moves past the end of the shroud, the part that is attached to the inner-shroud starts to wrap around the outer-shroud. As the wrap around progresses, the shock wave weakens and grows like an ellipsoid. A forebody attaching "leg" eventually develops, as shown in the pressure contours of Fig. 4 at 1050 μs. Eventually, the "leg" leaves the nose and the ellipsoid expands to infinity. That completes the propulsion physics of the Laser Lightcraft for a single pulse of laser energy.

The coupling coefficient is the generated impulse (N-s) divided by the delivered average laser single-pulse energy (MJ). It is a performance measure unique to the pulsed laser propulsion, and conceptually similar to the specific impulse (generated thrust divided by propellant weight flow rate) of a chemical rocket. Figure 5 shows a comparison of model predicted and experimental measured coupling coefficients for Model #200-3/4. The model with non-equilibrium radiation produced slightly better comparison than that without non-equilibrium radiation. The scattering of the measured data is attributed to the measurement of the laser energy, which varied from shot to shot (± 10 J) and an average over many pulses was used. The model (without non-equilibrium radiation) predicted coupling coefficients agree reasonably well with those measured in the laboratory. Figure 6 shows a comparison of model predicted and measured impulses for Model A. The model predicted slightly higher impulses at laser pulse energies from 600 to 800 J. It is anticipated that the comparison improves with inclusion of non-equilibrium calculation.

Figure 7 shows the predicted maximum electron density ($N_{e,max}$) as a function of elapsed time for Model #200-3/4. It rises sharply within about 5 μs, reaching its peak, then drops with time. The earliest rise and the highest peak value occur for the highest laser pulse energy (400 J), as expected. The computation indicates the occurrence of plasma resonance for all cases since the maximum electron densities exceed the critical value for about 25 to 45 μs.

Conclusions

A computational plasma aerodynamics model has been developed to study the propulsion physics of an experimental Laser Lightcraft. The model development is based on a building block approach such that the model can be improved continuously with improved understanding of the physics. The model predicted laser propulsion physics such as the optical breakdown and detonation wave propagation agree well with those described in the literature. The model predicted coupling coefficient for a Model #200-3/4 Laser Lightcraft and the predicted impulse for a Model A Laser Lightcraft agreed reasonably well with those measured.

Acknowledgments

The authors wish to thank Sandy Kirkindall of Laser Propulsion and John Cole of Advanced Propulsion for supporting this study. The lead author wishes to thank Chris Beairsto of the Directed Energy Team for the laser specifics, James Reilly of NorthEast Science and Technology and Jonathan Jones for discussions on plasma resonance, and Shen Zhu for discussions on the energy conversion processes during the plasma resonance.

References

[1] Kantrowitz, A., "Propulsion to Orbit by Ground-Based Lasers," *Astronautics and Aeronautics*, Vol. 10, No. 5, May 1972, pp. 74-76.

[2] Glumb, R.J., and Krier, H., "Concepts and Status of Laser-Supported Rocket Propulsion," *Journal of Spacecraft and Rockets*, Vol. 21, NO. 1, 1984, pp. 70-79.

[3] Brandstein, A., and Levy, Y., "Laser Propulsion System for Space Vehicles," *Journal of Propulsion and Power*, Vol. 14, No. 2, 1998, pp. 261-269.

[4] Jeng, San-Mou, and Keefer, Dennis, "Theoretical Evaluation of Laser-Sustained Plasma Thruster Performance," *Journal of Propulsion*, Vol. 5, No. 5, Sept-Oct., 1989, pp. 577-581.

[5] Molvik, G.A., Choi, D., and Merkle, C.L., "A Two-Dimensional Analysis of Laser Heat Addition in a Constant Absorptivity Gas," *AIAA Journal*, Vol. 23, No. 7, 1985, pp. 1053-1060.

[6] Myrabo, L., Raizer, Y.P., and Surzhikov, S.T., "Laser Combustion Waves in Laval Nozzles," *High Temperature*, Vol. 33, No. 1, 1995, pp. 11-20.

[7] Myrabo, L.N., Messitt, D.G., and Mead, F.B., Jr., "Ground and Flight Tests of a Laser Propelled Vehicle," AIAA Paper 98-1001, Jan., 1998.

[8] Mead, F.B., Jr., and Myrabo, L.N., Messitt, D.G., "Flight and Ground Tests of a Laser-Boosted Vehicle," AIAA Paper 98-3735, July, 1998.

[9] Raizer, Y.P., "Subsonic Propagation of a Light Spark and Threshold Conditions for the Maintenance of Plasma by Radiation," *Soviet Physics JETP*, Vol. 31, Dec., 1970, pp. 1148-1154.

[10] Kemp, N.H., and Root, R.G., "Analytical Study of LSC Waves in Hydrogen," *Journal of Energy*, Vol. 3, Jan-Feb, 1979, pp. 40-49.

[11] Barth, T.J., "Recent Developments in High Order K-Exact Reconstruction on Unstructured Meshes," AIAA Paper 93-0668, 1993.

[12] Fletcher, R., "Conjugate Gradient Methods for Indefinite Systems," *Lecture Notes in Mathematics*, Vol. 506, 1976, pp. 73-89.
[13] Saad, Y., and Schultz, M.H., "GMRES: A Generalized Minimal Residual Algorithm for Solving Nonsymmetric Linear Systems," *SIAM Journal of Scientific and Statistical Computing*.
Vol. 7, No. 3, Jan. 1986, pp. 856-869.
[14] Landau, L., and Teller, E., "Zur Theorie der Schalldispersion," Physic Z. Sowjetunion, Vol. 10, No. 34, 1936.
[15] Park, C., "Review of Chemical-Kinetic Problems of Future NASA Missions, I: Earth Entries," *Journal of Thermophysics and Heat Transfer*, Vol. 7, No. 3, 1993, pp. 385–398.
[16] Ergun, M.A., *Modeling and Experimental Measurements of Laser Sustained Hydrogen Plasmas*, Ph.D. Dissertation, University of Illinois at Urbana-Champaign, 1993.
[17] Raizer, Y.P., and Tybulewicz, A., "Laser-Induced Discharge Phenomena", *Studies in Soviet Science*, Edited by Vlases, G.C., and Pietrzyk, Z.A., Consultants Bureau, New York, 1977.
[18] Edwards, A. L. and Fleck, Jr. J. A., "Two-dimensional Modeling of Aerosol-Induced Breakdown," *Journal of Applied Physics*., Vol. 50, No. 6, 1979, pp. 4307-4313.
[19] Modest, M. F., "Radiative Heat Transfer," McGraw-Hill, NY, 1993.
[20] Park, C., "Nonequilibrium Air Radiation Program: User's Manual," NASA TM-86707, 1985.
[21] Hartung, Lin, "Theory and User's Manual for Loran Code," NASA TM-4564, 1994.
[22] Gogel, T. H., Duouis, M., and Messerschmid, E. W., " Radiation Transport Calculation in High Enthalpy Environment for Two-dimensional Axisymmetric Geometries," *Journal of Thermophysics and Heat Transfer*, Vol. 8, No. 4, 1994, pp. 744-750.
[23] Hartung, L. C. and Hassan, H. A., "Radiation Transport around Axisymmetric Blunt Body Vehicles Using a Modified Differential Approximation," *Journal of Thermophysics and Heat Transfer*, Vol. 7, No. 2, 1993, pp. 220-227.
[24] Surzhikov, S. T., "Calculation of the Radiation Flux Divergence near the Region of Local Heat Release by Quadromoment Method," Proceedings of the First International Symposium on Radiation Transfer, Kusadasi, Turkey, August 13-18, 1995, pp. 92-106.
[25] Liu, J., Shang, H., Chen, Y.-S., and Wang, T.-S., "Analysis of Discrete Ordinates Method with Even Parity Formulation," *Journal of Thermophysis and Heat Transfer*, Vol. 11, No. 2, April-June, 1997, pp. 253-260.
[26] Coelho, P. J. and Carvalho, M. G., "A Conservative Formulation of the Discrete Transfer Method," *Journal of Heat Transfer*, Vol. 119, No. 1, 1997, pp. 118-128.
[27] Brown, Sanborn C., *Basic Data of Plasma Physics*, The Technology Press of The Massachusetts Institute of Technology and John Wiley & Sons, Inc., New York.
[28] Hora, Heinrich, *Laser Plasmas and Nuclear Energy*, Plenum Press, New York and London, 1975.
[29] Zhu, S., USRA, MSFC, personal communication.
[30] Lyons, P.W., Myrabo, L.N., Jones, R.A., Nagamatsu, H.T., and Manka, C., "Experimental Investigation of a Unique Airbreathing Pulsed Laser Propulsion Concept," AIAA Paper 91-1922, 1991.
[31] Chen, Y.S., "UNIC-MESH: A Model Builder & Mesh Generator, Graphical User Interface," Engineering Sciences, Inc. Internal Report, UNIC-Mesh-V.3.0, 2000.
[32] Wang, T.-S., "Numerical Study of the Transient Nozzle Flow Separation of Liquid Rocket Engines," *Computational Fluid Dynamics Journal*, Vol.1, No.3, Oct. 1992, pp. 319-328.
[33] Wang, T.-S. and Chen Y.-S., "Unified Navier-Stokes Flowfield and Performance Analysis of Liquid Rocket Engines," *Journal of Propulsion and Power*, Vol. 9, No. 5, Sept.-Oct. 1993, pp.678-685.
[34] Park, C., *Nonequilibrium Hypersonic Aerothermodynamics*, Wiley, New York, 1990.
[35] Sharma, S.P., Gillespie, W.D., and Meyer, S.A., "Shock Front Radiation Measurements in Air," AIAA Paper 91-0573, Jan. 1991.

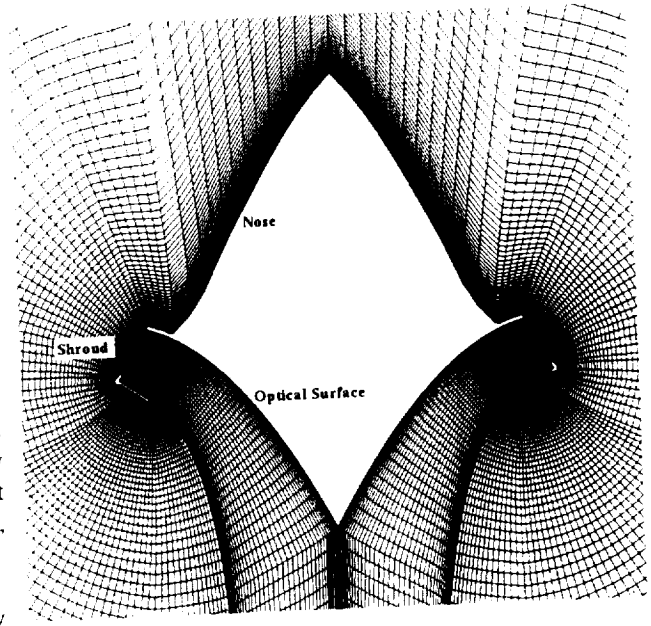

Fig. 1 The layout of a computational grid for the laser lightcraft.

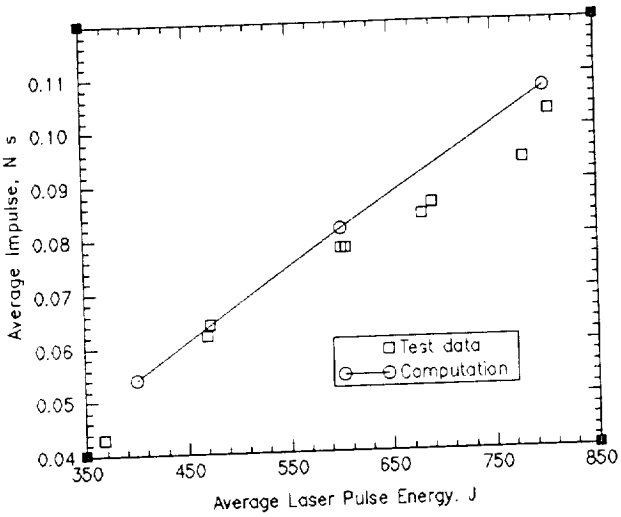

Fig. 6 A comparison of the impulses.

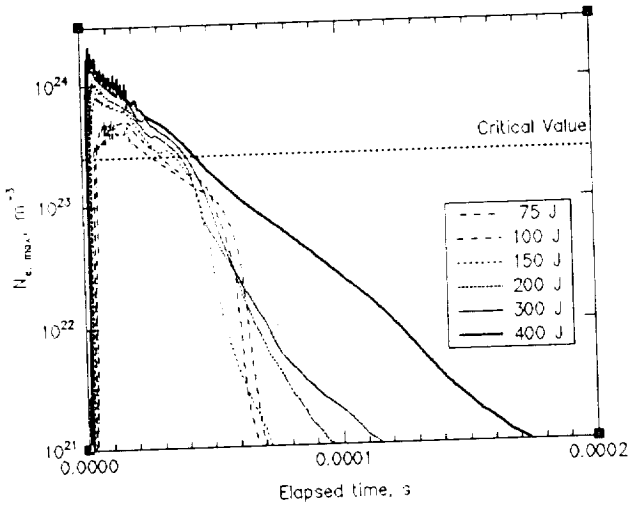

Fig. 7 Computed maximum electron density history.